Nanoscale

PAPER

View Article Online
View Journal | View Issue



Cite this: *Nanoscale*, 2024, **16**, 9791

# Multi-atomic loaded $C_2N_1$ catalysts for $CO_2$ reduction to CO or formic acid†

Yimeng Sun,[a] Lin Tao, *[a] Mingjie Wu,*[b] Davoud Dastan,[c] Javed Rehman, [d] Lixiang Li [a] and Baigang An*[a]

In recent years, the development of highly active and selective electrocatalysts for the electrochemical reduction of $CO_2$ to produce CO and formic acid has aroused great interest, and can reduce environmental pollution and greenhouse gas emissions. Due to the high utilization of atoms, atom-dispersed catalysts are widely used in $CO_2$ reduction reactions ($CO_2$RRs). Compared with single-atom catalysts (SACs), multi-atom catalysts have more flexible active sites, unique electronic structures and synergistic interatomic interactions, which have great potential in improving the catalytic performance. In this study, we established a single-layer nitrogen–graphene-supported transition metal catalyst (TM-$C_2N_1$) based on density functional theory, facilitating the reduction of $CO_2$ to CO or HCOOH with single-atom and multi-atomic catalysts. For the first time, the TM-$C_2N_1$ monolayer was systematically screened for its catalytic activity with *ab initio* molecular dynamics, density of states, and charge density, confirming the stability of the TM-$C_2N_1$ catalyst structure. Furthermore, the Gibbs free energy and electronic structure analysis of 3TM-$C_2N_1$ revealed excellent catalytic performance for CO and HCOOH in the $CO_2$RR with a lower limiting potential. Importantly, this work highlights the moderate adsorption energy of the intermediate on 3TM-$C_2N_1$. It is particularly noteworthy that 3Mo-$C_2N_1$ exhibited the best catalytic performance for CO, with a limiting potential ($U_L$) of −0.62 V, while 3Ti-$C_2N_1$ showed the best performance for HCOOH, with a corresponding $U_L$ of −0.18 V. Additionally, 3TM-$C_2N_1$ significantly inhibited competitive hydrogen evolution reactions. We emphasize the crucial role of the d-band center in determining products, as well as the activity and selectivity of triple-atom catalysts in the $CO_2$RR. This theoretical research not only advances our understanding of multi-atomic catalysts, but also offers new avenues for promoting sustainable $CO_2$ conversion.

Received 13th March 2024,
Accepted 19th April 2024

DOI: 10.1039/d4nr01082e

rsc.li/nanoscale



## 1. Introduction

The increase in fossil fuel consumption leads to the accumulation of $CO_2$ in the atmosphere, causing serious environmental problems such as the greenhouse effect and ocean acidification, forcing people to find effective ways to reduce the concentration of $CO_2$ in the atmosphere and promote green and low-carbon development.[1–5] In recent years, a variety of efficient $CO_2$ conversion technologies have been developed, including biocatalysis, photocatalysis, and electrocatalysis.[6–8] Among them, the electrocatalytic $CO_2$ reduction reaction ($CO_2$RR) has attracted extensive attention as a promising approach.[3,9] However, the excellent thermodynamic stability and high activation barrier of $CO_2$ make the reaction more difficult.[10] In addition, the hydrogen evolution reaction (HER) is a competitive side reaction of the $CO_2$RR because it has a low overpotential.[11] Therefore, it is of great significance to design a novel $CO_2$RR electrocatalyst with a low overpotential and HER inhibition.

In recent years, due to the development of nanotechnology, it is possible to fine-tune the structure of an electrocatalyst at the nanoscale to control the structure of the electrocatalyst, making it have better stability, catalytic activity, and product selectivity. Single-atom catalysts (SACs) with isolated transition metal (TM) atoms stabilized by carbon-based materials have attracted more and more attention due to their special electronic structure and platform utilization[12] and have become promising candidate materials in the nitrogen reduction reaction,[13] HER,[14–16] oxygen reduction reaction,[15,17] oxygen evol-

[a]*School of Chemical Engineering, University of Science and Technology Liaoning, Anshan 114051, China. E-mail: taolin@ustl.edu.cn, bgan@ustl.edu.cn*
[b]*State Key Laboratory of New Textile Materials and Advanced Processing Technologies, Wuhan Textile University, Wuhan 430200, China. E-mail: mjwu@wtu.edu.cn*
[c]*Department of Materials Science and Engineering, Cornell University, Ithaca, NY 14850, USA*
[d]*State Key Laboratory of Metastable Materials Science and Technology, Yanshan University, Qinhuangdao 066004, China*

† Electronic supplementary information (ESI) available. See DOI: https://doi.org/10.1039/d4nr01082e

ution reaction,[18,19] $CO_2$RR,[20,21] and other reactions.[22] Previous studies have indicated that catalysts such as Mn, Mo, Ru, and Ti offer distinct advantages in the $CO_2$RR compared to the HER, requiring lower overpotentials for the generation of intermediate products (*COOH or *OCHO).[23–29] Unfortunately, the stability of SACs is not satisfactory,[30] because when the bond of individual atoms to the carrier is weak, they tend to aggregate into nanoparticles, which inevitably affects their catalytic activity and further hinders their practical application.

In contrast, single-cluster catalysts (SCCs) supported in single-layer nitrogen–graphene have great potential to advance the design and manufacture of high-performance catalysts due to their tunable electronic structure and adaptable active sites and have shown superiority in terms of stability, and are widely regarded as promising alternatives to SACs.[31] The $C_3N_1$ monolayer is a two-dimensional material with periodic uniform cavities, and is a derivative of nitrogen-doped graphene. Its cavity is surrounded by 6 nitrogen atoms and is considered an ideal carrier for transition metal loading. Its high thermal stability facilitates the synthesis of stable transition metal catalysts.[32–34]

Among SCCs, dual-atomic catalysts (DACs) have been extensively studied and are considered a new frontier.[35–38] Chen *et al.*[37] reported that DACs have the smallest metal alloy size and the largest atom utilization and exhibit excellent performance in various electrocatalytic reactions. In DACs, the binding strength of several intermediates can be optimized simultaneously to achieve multi-intermediate reactions. Zhang *et al.*[9] found that the combination of diatomic metal and nonmetal sites disrupted the electron density symmetry of the local coordination environment, and the formed symmetrical break sites improved the adsorption of key intermediates (such as *COOH and *OCHO). Wang *et al.*[39] demonstrated that a unique dual $Fe_2$–$N_6$ catalyst showed the electrocatalytic reduction of $CO_2$ to CO configuration, outstanding intrinsic activity, selectivity, and durability compared to SACs. Additionally, Mn and Mo, serving as DACs, are situated at the center and exhibit a polarized bond interaction with $CO_2$, underscoring the role of metal-centered catalysts in $CO_2$ and substrate interactions.[40,41] DACs break the structural relationship constructed in traditional metal catalysts and improve the catalytic activity of the catalyst to form higher-order carbon products.[42–44]

Furthermore, triple-atom catalysts (TACs) have attracted much attention as a deeper extension of SACs. First, they exhibit a higher loading capacity for metal atoms and are able to get closer to the active site.[45] The formation of metal–metal bonds or metal–bridge atomic bonds provides a strategic means to control the electron synergistic adsorption of various reactants and intermediates.[46,47] TACs can provide a wider variety of asymmetric adsorption sites. These sites are particularly suitable for more complex catalytic processes involving multiple reaction steps and intermediates, and the synergy between the three atoms can also modulate the d-band electronic structure, thereby enhancing the catalytic performance.[45,48,49] Jia *et al.*[50] reported that TACs, as powerful electrocatalysts for the $CO_2$RR, provide a large number of active sites, and also have a large electrochemical surface area and rapid charge transfer, which improves the reaction rate. Liu *et al.*[51] found that TACs have abundant active sites for the $CO_2$RR. their catalytic performance can be enhanced by the interaction of adjacent active sites. In particular, metals such as Mn, Mo, Ru, *etc.*, as catalysts, demonstrate promising experimental feasibility and stable catalytic performance. They effectively suppress the HER while exhibiting excellent selectivity in the $CO_2$RR.[45,52,53]

As excellent $CO_2$RR catalysts, both single atoms and single clusters demonstrate outstanding catalytic performance. However, the effect of the number of metal atoms on the structure–activity relationship of the catalyst is still unclear. In addition, previous studies have inconsistently described the catalytic properties of catalysts loaded with Mn, Mo, Ru, and Ti. Therefore, it is necessary to systematically analyze the catalytic performance of $CO_2$ using the above metal atoms and their numbers and provide theoretical guidance for the rational design of low-cost high-performance catalysts.

In this work, density functional theory (DFT) calculations were employed to reveal the structures of single atoms and single clusters composed of four metal elements (Mn, Mo, Ru, and Ti), which were loaded onto $C_2N_1$ monolayer materials as catalysts for $CO_2$ electrochemical reduction. First, the stability and conductivity of TM-$C_2N_1$ were investigated through the analysis of its electronic structure, density of states (DOS), and *ab initio* molecular dynamics (AIMD). Second, the adsorption and activation effect of TM-$C_2N_1$ on $CO_2$ were explored, focusing on the $CO_2$ configuration, adsorption energy comparison with $H_2O$, and the competitive adsorption relationship between the $CO_2$RR and HER. Finally, to better understand the preferred pathways for $CO_2$ reduction to CO or HCOOH on TM-$C_2N_1$, calculations were conducted for Gibbs free energy, limiting potential, overpotential, and Crystal Orbital Hamiltonian Population (COHP). The results show that the 3TM-$C_2N_1$ catalyst has a stable structure, can effectively adsorb and activate $CO_2$, and has optimal inhibition performance for the HER. Among them, 3Mo-$C_2N_1$ and 3Ti-$C_2N_1$ had the best catalytic activity for CO and HCOOH, in the $CO_2$RR with limiting potentials of −0.62 V and −0.42 V, respectively. These findings not only provide a theoretical basis for the experimental regulation of $C_2N_1$-based catalysts, but also have guiding significance for the development of other high-efficiency $CO_2$RR electrocatalysts.

## 2. Results and discussion

### 2.1 Structural stability

In this section, first, in order to clearly understand the electrocatalytic process of $CO_2$ for materials with different types of atoms and different numbers of atoms, a schematic diagram is shown, as shown in Fig. 1a. It shows the reduction pathways of $CO_2$ at different catalytic sites. Second, all transition metal single-atom catalysts and single-cluster catalyst structures sup-

 

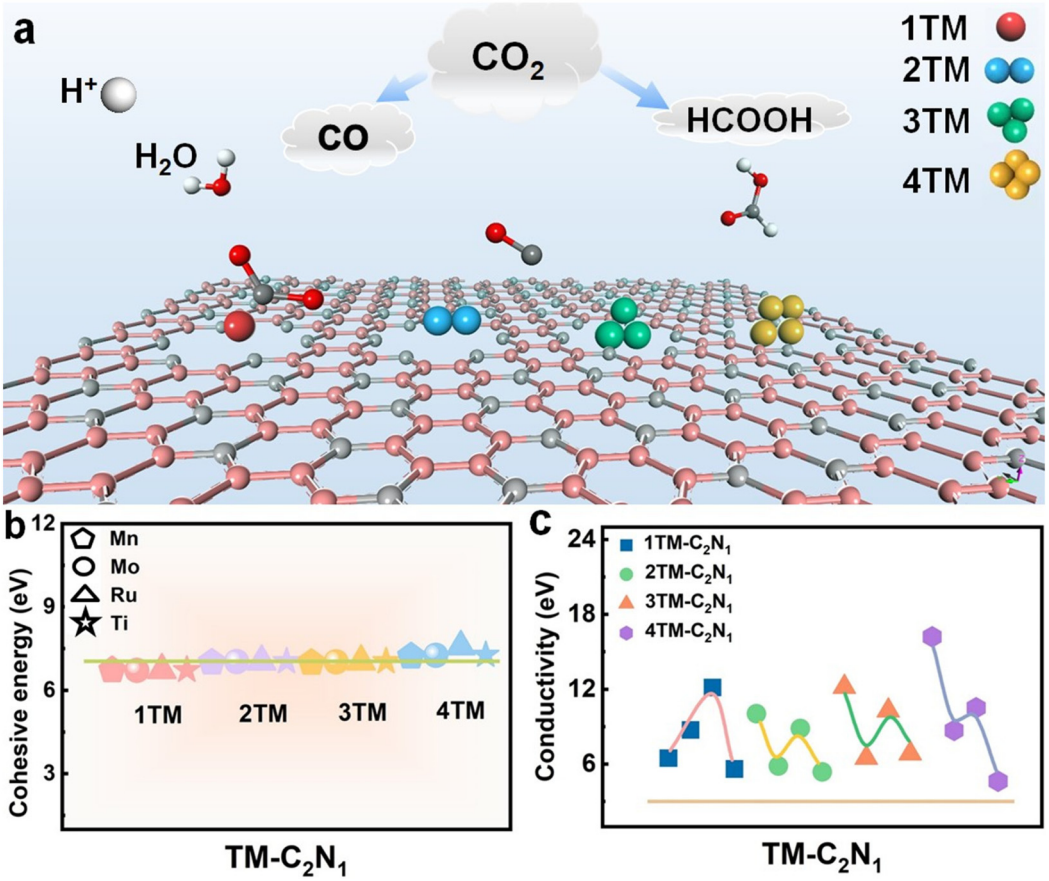


**Fig. 1** (a) Schematics of $C_2N_1$ with TM loads facilitates $CO_2$ conversion. (b) Cohesion energy of the TM-$C_2N_1$ monolayer. (c) The height of the DOS curve for TM-$C_2N_1$ at the Fermi level. The order of data points in (b) and (c) is Mn, Mo, Ru, and Ti.

ported on N-doped graphene were constructed, and the optimized structures are shown in Fig. S1–S4.† Then, in order to evaluate the stability of the TM-$C_2N_1$ structure, the cohesion energy, charge density, and AIMD were calculated to study the stable structure. Finally, the heights of DOS curves for the TM-$C_2N_1$ and $C_3N_1$ monolayers were calculated as the key parameters for the conductivity of the catalyst. The TM-$C_2N_1$ model uses a 5 × 5 supercell of the $C_3N_1$ monolayer, and there are a total of 54 C atoms and 18 N atoms in the model, as shown in Fig. S1–S4,† and we set a vacuum layer of 20 Å in the $z$ direction to avoid the influence between adjacent lattices. The transition metal was placed in the N6 cavity to form the TM-$C_2N_1$ configuration.

High stability is a prerequisite for catalyst applications, so we evaluated the stability of TM-$C_2N_1$ catalysts with cohesive energy. The higher the cohesion energy, the more stable the corresponding structure.[54–56] Cohesion energy ($E_{coh}$) can be calculated according to the following formula:[2]

$$E_{coh} = \frac{n_1 E_{TM} + n_2 E_C + n_3 E_N - E_{C_2N}}{n_1 + n_2 + n_3} \quad (1)$$

where $E_C$ and $E_N$ denote the energies (eV) of C and N atoms, respectively. $n_1$, $n_2$, and $n_3$ are the number of metals and C and N atoms. As shown in Fig. 1b, based on the calculation results of cohesion energy, it can be found that the cohesion energies of 1TM-$C_2N_1$, 2TM-$C_2N_1$, 3TM-$C_2N_1$, and 4TM-$C_2N_1$ materials are relatively concentrated. The cohesion energies of Mn-$C_2N_1$, Mo-$C_2N_1$, Ru-$C_2N_1$, Ti-$C_2N_1$, 2Mn-$C_2N_1$, and 3Mn-$C_2N_1$ are slightly smaller than that of the initial $C_3N_1$ monolayer (7.03 eV per atom) but higher than those of carbon phosphide (4.12–6.45 eV per atom) and silane (3.71 eV per atom).[11] The cohesion energies of the remaining 10 metal catalysts were all greater than or equal to that of the initial $C_3N_1$ monolayer. Hence, these findings demonstrate the remarkable stability of all TM-$C_2N_1$ configurations.

To better understand the interaction between the TM and the monolayer, we calculated the charge density of TM-$C_2N_1$, and the charge density diagram in Fig. S5–S8† show that the positive charge accumulates around the metal atom and decreases around the N atom, indicating that the electrons are transferred from the metal atom to the N atom, allowing the N atom to bind the TM atom. In addition, in order to judge the stability of the TM-$C_2N_1$ structure from the thermodynamic properties, AIMD simulation was carried out. It was calculated that the AIMD runs at 500 K for 10 ps and outputs a structure file every 10 fs. The detailed calculations are shown in Fig. S9–S12.† The results show that these materials are able to maintain good stability.

Finally, in order to explore the conductivity of the catalyst, the height of the DOS curve at the Fermi level for the TM-$C_2N_1$ monolayer represents the conductivity of the catalyst.[2,57–62] DOSs were calculated as the key parameters of catalyst conductivity. As shown in Fig. 1c, the DOS height for TM-$C_2N_1$ is higher than that of $C_3N_1$, demonstrating that the conductivity is improved after the introduction of loaded metals. The detailed calculations are shown in Fig. S5–S8,† and the overall DOS shows that after the introduction of the TM, the curve around the Fermi level increases slightly, indicating that the conductivity of the material has improved. In addition, partial density of states (PDOS) calculations were performed to study the behavior of the doped TM in depth. There were obvious overlapping peaks between the d orbital of the TM and the p orbital of the N of the substrate, indicating that the interaction between the TM and the substrate was stronger. The TM can be firmly attached to the $C_3N_1$ monolayer. This indicates that there is an interaction between the loaded TM atoms and the substrate, ensuring its structural stability.

### 2.2 Activation and selectivity

In this section, to understand the catalytic performance of catalysts and the advantages of $CO_2$RR development, the d-band center and activation degree of $CO_2$ were studied first, and second, the adsorption energies of $CO_2$ and $H_2O$ were calculated as important references. In addition, we further compared $\Delta G$(*COOH) and $\Delta G$(*OCHO) with $\Delta G$(*H). Further screening of the good TM-$C_2N_1$ catalyst ensures the normal $CO_2$RR.

$CO_2$ adsorption is the first and crucial step in the $CO_2$RR. Stable $CO_2$ adsorption is a prerequisite for the continuation of the $CO_2$RR. The degree of $CO_2$ activation reflects the catalytic performance of the catalyst to a certain extent. As shown in Fig. S13† ($CO_2$ planar three-dimensional structure display), $CO_2$ can be stably adsorbed on the surface of the catalyst, and the molecular configuration of $CO_2$ has changed significantly, indicating that $CO_2$ has been initially activated. In addition, in order to more intuitively observe the degree of activation and conductivity, as well as charge accumulation and consumption during the interaction between $CO_2$ and TM-$C_2N_1$, the results of charge density analysis are shown in Fig. S13† and the DOSs are shown in Fig. S14–S17.† The results show that TM-$C_2N_1$ transfers a large amount of charge during gas adsorption. A distinct red color is observed around the $CO_2$, which clearly indicates that the $CO_2$ acquires electrons from TM-$C_2N_1$, indicating that there is an interaction between $CO_2$ and TM-$C_2N_1$. Moreover, the p-orbital anchoring of C in the activated $CO_2$ and the d-orbital of the transition metal in TM-$C_2N_1$ have a hybridization effect, indicating that there is an interaction between $CO_2$ and TM-$C_2N_1$. For quantitative analysis, information such as the $CO_2$ adsorption energy and $CO_2$ bond length angle are listed in Table S1.† The smaller the bond angle, the stronger the degree of activation. The change of C–O bond length from 1.18–1.32 Å and the bending of O–C–O bond angle from 127.19°–163.22° (Fig. 2a) indicate that $CO_2$ has been effectively activated.

In order to explore the potential mechanism of the adsorption reaction of $CO_2$ on the surface of the catalyst, we calculated the d-band center of TM-$C_2N_1$ because it can reflect the interaction between the gas molecules and the TM atoms on the surface. Fig. 2b shows that the d-band center of TM-$C_2N_1$ has a linear relationship with the adsorption energy, and the correlation coefficient is in good agreement with the theoretical model of the d-band center. Thus, the elevation of antibonding orbitals contributes to an increase in the adsorption energy.

It is well known that the kinetically prone HER hinders the progress of the $CO_2$RR as a side reaction. So a good catalyst to inhibit the HER is necessary. First, we calculated the reaction mechanism of the HER by adsorbing $H_2O$, because the $CO_2$RR tends to be performed in neutral or alkaline electrolytes. Fig. 2c shows the stark contrast between the adsorption energies of $H_2O$ and $CO_2$. Due to $|E_{ads}(H_2O)| < |E_{ads}(CO_2)|$, *$CO_2$ is more easily adsorbed on the surface of TM-$C_2N_1$ catalysts than *H, thereby inhibiting the HER. Therefore, $CO_2$ rather than $H_2O$ first occupies the active sites on the surface of TM-$C_2N_1$, promoting the $CO_2$RR as the main reaction on these 13 catalysts. Please refer to Tables S1 and S2† for details on the adsorption energy of $H_2O$ and $CO_2$.Moreover, during the first protonation process, the hydrogenation of $CO_2$ produces two intermediates *COOH and *OCHO. As shown in Fig. S18,† by comparing $\Delta G$(*COOH) and $\Delta G$(*OCHO) with $\Delta G$(*H), the 2/3TM-$C_2N_1$ catalysts all fall in the lower right half region ($CO_2$RR selective), which tends to produce *COOH or *OCHO. Combining the above two points, it can be concluded that the 2/3TM-$C_2N_1$ catalyst is selective to the $CO_2$RR and can well inhibit the occurrence of the HER. Therefore, the $CO_2$RR has a clear advantage over the HER under electrochemical conditions.

The diffusion performance of $CO_2$ on the catalyst material surface dictates the reaction rate.[63,64] Therefore, to explore the performance of catalysts in practical applications, molecular dynamics simulations were employed to calculate the diffusion coefficients of $CO_2$ on different material surfaces, thereby obtaining diffusion performance. Fig. S19–S22† depict snapshots of all catalysts capturing $CO_2$ at equilibrium. First, the mean-squared displacement (MSD) of TM-$C_2N_1$ was calculated, as shown in Fig. 2d. The results display that 3TM-$C_2N_1$ has the smallest diffusion performance based on the slopes. Furthermore, diffusion coefficients can be obtained through the Einstein diffusion equation. The detailed data are shown in Table S3.† The diffusion coefficients of 3Mn-$C_2N_1$, 3Mo-$C_2N_1$, 3Ru-$C_2N_1$ and 3Ti-$C_2N_1$ were 2.91, 2.19, 3.86 and 2.78, respectively. Among which, 3Mo-$C_2N_1$ and 3Ti-$C_2N_1$ had the best diffusion performance. The diffusion coefficient has an effect on the diffusion of $CO_2$ on the surface, and the smaller the diffusion coefficient, the more stable the $CO_2$ adsorption and the better the catalytic effect.

### 2.3 $CO_2$ reduction to CO or HCOOH

In this section, we first present the intermediate structure of the $CO_2$ reduction process to CO and HCOOH, followed by the calculation of the free energy for each corresponding structure.

 

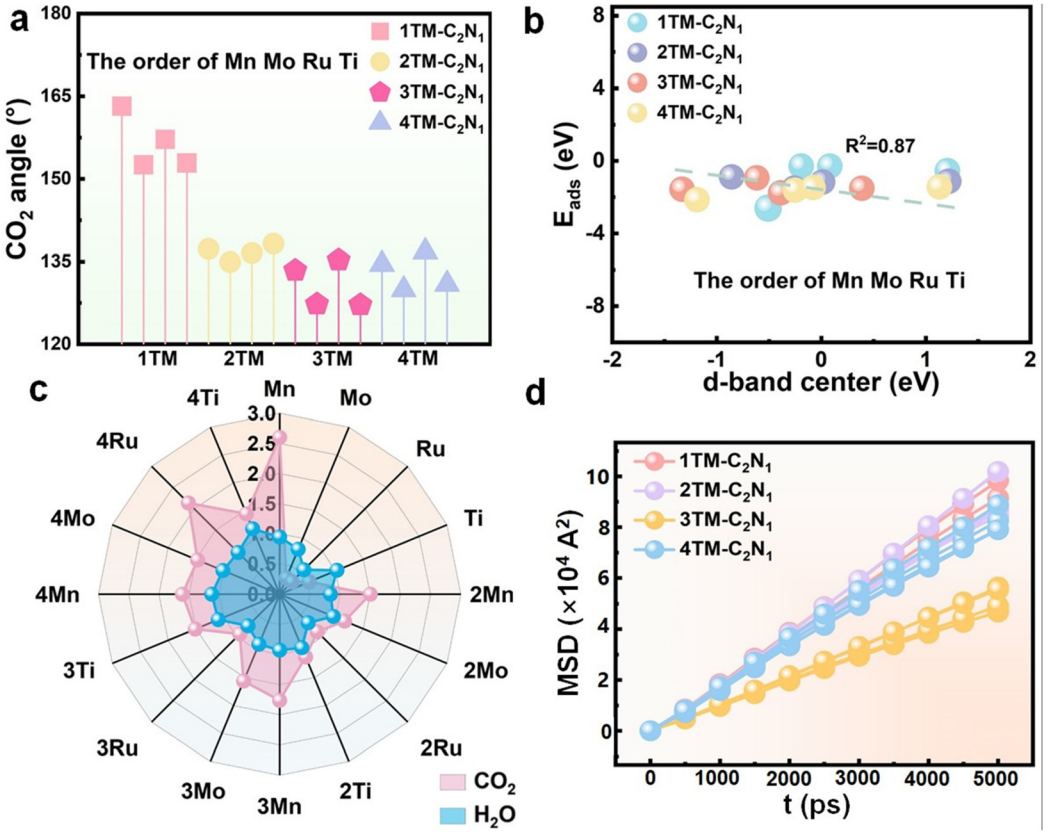


**Fig. 2** (a) $CO_2$ activation angle on TM-$C_2N_1$. (b) Linear relationship between the d-band center of TM-$C_2N_1$ and the adsorption energy of $CO_2$. (c) Comparison of $H_2O$ and $CO_2$ adsorption energies on the TM-$C_2N_1$ monolayer. (d) Diffusion of $CO_2$ on the TM-$C_2N_1$ monolayer.

Finally, we conducted free energy calculations for the reaction pathway. The path of $CO_2$ to CO on TM-$C_2N_1$ is: $CO_2$ → *$CO_2$ → *COOH → *CO → CO. For HCOOH generation, the $CO_2$ to HCOOH generation path on TM-$C_2N_1$ is $CO_2$ → *$CO_2$ → *OCHO → *HCOOH → HCOOH. Fig. 3 shows the adsorption structure and free energy distribution of $CO_2$ intermediates to generate CO and HCOOH *via* a 2-electron path on the 3TM-$C_2N_1$ catalyst.

Regarding the CO product, 3Mn-$C_2N_1$ has a $CO_2$ → *COOH speed-limiting step and the Gibbs free energy variation is 0.63 eV. For the 3Mo-$C_2N_1$ catalyst, the speed-limiting step is $CO_2$ → *COOH and the maximum Gibbs free energy variation is 0.62 eV. Besides, for the 3Ru-$C_2N_1$ monolayer, the speed-limiting step is $CO_2$ → *COOH and the maximum Gibbs free energy variation is 0.92 eV. Finally, 3Ti-$C_2N_1$ has a $CO_2$ → *COOH speed-limiting step and the maximum Gibbs free energy variation is 1.15 eV. For the production of HCOOH, first, 3Mn-$C_2N_1$ has a rate-limiting step of $CO_2$ → *OCHO and a Gibbs free energy variation maximum of 0.91 eV. Then, 3Mo-$C_2N_1$ has a $CO_2$ → *OCHO rate-limiting step and a maximum Gibbs free energy variation of 0.93 eV. 3Ru-$C_2N_1$ has a $CO_2$ → *OCHO rate-limiting step and a maximum Gibbs free energy variation of 1.39 eV. Finally, for 3Ti-$C_2N_1$, the rate-limiting step is *OCHO → *HCOOH and the maximum variation of Gibbs free energy is 0.42 eV. Furthermore, these results have also been validated by the dynamic barrier of elementary steps. Thus, the rate-limiting step was elucidated based on both thermodynamic and kinetic processes.

It is worth noting that 1TM-$C_2N_1$, 2TM-$C_2N_1$, and 4TM-$C_2N_1$ generate CO or HCOOH paths and rate-limiting steps are presented in Fig. S23–S25.† The Gibbs free energy of 1TM-$C_2N_1$ varies greatly overall, and for the CO product, Mn-$C_2N_1$ has a $CO_2$ → *COOH rate-limiting step with a maximum free energy difference of 4.83 eV. For HCOOH products, Ru-$C_2N_1$ has a $CO_2$ → *OCHO rate-limiting step with a maximum free energy difference of 3.78 eV. For the CO product, 4Ti-$C_2N_1$ has a $CO_2$ → *COOH speed-limiting ladder, and the Gibbs free energy becomes 2.18 eV. With regard to the HCOOH product, 4Mn-$C_2N_1$ has a $CO_2$→*OCHO rate-limiting step and a Gibbs free energy change of 1.28 eV. Among them, for CO, 3Mo-$C_2N_1$ has the smallest free energy difference, making it the best CO catalyst. For HCOOH, 3Ti-$C_2N_1$ has the smallest free energy difference and is the most effective catalyst for HCOOH generation, so 3Mo-$C_2N_1$ and 3Ti-$C_2N_1$ exhibit excellent performance.

### 2.4 Catalytic performance

For a quantitative analysis and clear comparison of catalytic performance, Fig. S26 and S27† show the limiting potential ($U_L$) and overpotential ($\eta$) of $CO_2$ reduction to CO or HCOOH on TM-$C_2N_1$. The results demonstrate that TACs exhibit the

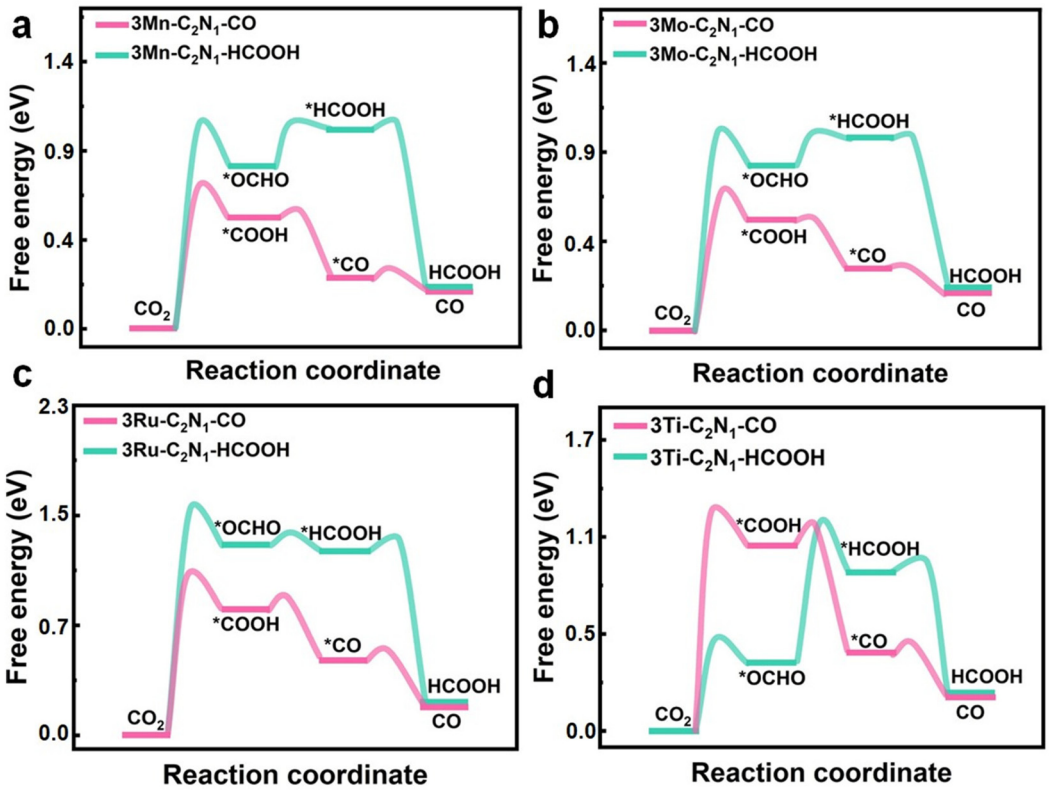


**Fig. 3** Gibbs free energy distribution diagram of the $CO_2$ reduction pathway toward CO or HCOOH on (a) 3Mn-$C_2N_1$, (b) 3Mo-$C_2N_1$, (c) 3Ru-$C_2N_1$, and (d) 3Ti-$C_2N_1$.

best catalytic performance, based on the smallest overpotential, compared to other single-atom and multi-atom catalysts. Among them, the 3Mo/3Ti-$C_2N_1$ catalyst shows the optimal catalytic performance, as indicated by the minimal $\eta$ for the formation of CO and HCOOH products. This parameter determines the energy cost in experiments. The impact of product separation on catalytic rates cannot be overlooked, as higher adsorption energy makes desorption more challenging. Therefore, establishing the relationship between the catalytic performance (overpotential) and the product adsorption energy is of significant importance for a deeper understanding of the structure–performance relationship of catalysts.

As shown in Fig. 4a, for CO, 3Mo-$C_2N_1$ exhibits the best performance with a limiting potential of CO generation at 0.62 V. This indicates good catalytic activity and the lowest energy requirement. The vertices of the volcano plot represent the moderate adsorption energy of the product and therefore have the best catalytic performance. Conversely, as illustrated in Fig. 4b, 3Ti-$C_2N_1$ demonstrates the best overall performance for HCOOH generation. The limiting potential for the formation of HCOOH on 3Ti-$C_2N_1$ is 0.42 V; the results show that moderate adsorption can ensure a high yield of HCOOH. When $|U_L| > 0.9$ V, it suggests that the reaction requires a significant amount of energy absorption, making it less likely to occur. The analysis suggests that the $CO_2$RR catalyzed by TM-$C_2N_1$ is feasible, with 3TM-$C_2N_1$ being the optimal catalyst for achieving efficient $CO_2$RR performance.

The catalytic performance of 3Mn-$C_2N_1$ is also very good, and the $U_L$ of CO generation is 0.63 V, which is only 0.01 V higher than the that of 3Mo-$C_2N_1$. The catalyst with the best performance to generate HCOOH is 3Ti-$C_2N_1$. The $U_L$ for generating HCOOH on 3Ti-$C_2N_1$ is 0.42 V, which exhibits good catalytic activity and is the lowest energy required among the four catalysts. The analysis shows that the 3TM-$C_2N_1$-catalyzed $CO_2$RR is achievable. Our work explores the excellent performance of TM-$C_2N_1$ for deep hydrogenation of $CO_2$ under electrocatalysis at lower electrode potentials. In the formation of CO and HCOOH, 3Mo-$C_2N_1$ and 3Ti-$C_2N_1$ have the best performance among the 13 catalysts. This result demonstrates the optimal potential of TAC catalysts supported by the $C_2N_1$ monolayer for the $CO_2$RR. Therefore, when $CO_2$ is reduced to CO and HCOOH, 3Mo-$C_2N_1$ and 3Ti-$C_2N_1$ have the best catalytic performance.

### 2.5 Catalytic mechanism

To gain insight into why the catalyst performance of the 3Mo-$C_2N_1$ and 3Ti-$C_2N_1$ monolayers is the best, we analyzed the key intermediates, which interact with the catalytically active site, from a molecular orbital perspective. It is the bonding orbital that plays a key role in the adsorption according to previous studies.[36,65–69] First of all, the interaction should not be too strong, which will lead to a sudden increase in the energy barrier of the next step, forming a restrictive link. Second, the interaction should not be too weak, which will lead to a

 

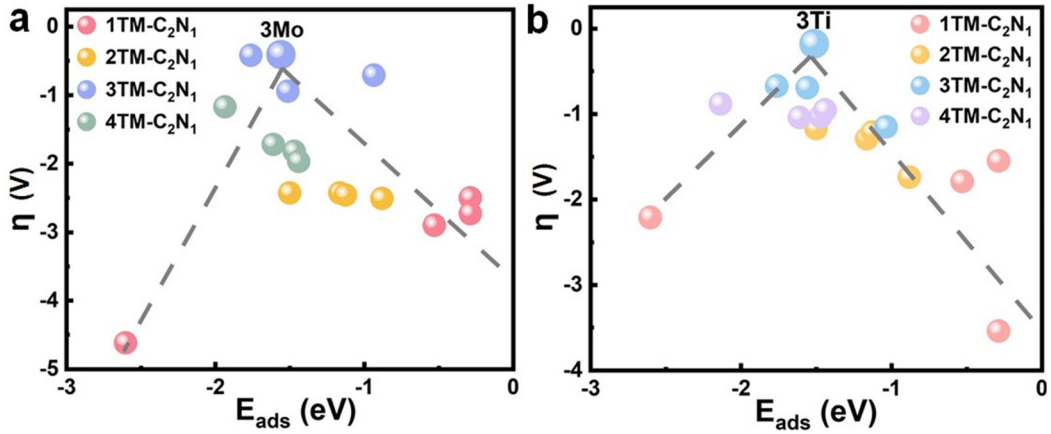


**Fig. 4** Relationship between the adsorption energy and the overpotential of products on TM-$C_2N_1$. (a) CO adsorbed on TM-$C_2N_1$. (b) HCOOH adsorbed on TM-$C_2N_1$.

decrease in the catalytic effect of the catalyst and make the catalyst fail. Hence, maintaining a moderate interaction is essential to obtain high-performance catalysts. To achieve this, we conducted COHP calculations for reducing the intermediates of the TM catalysts exhibiting the best performance.

Fig. S29 and S30† depict the most stable adsorption configuration, charge density distribution, and corresponding DOS of *COOH and *OCHO adsorption on 3Mo-$C_2N_1$ and 3Ti-$C_2N_1$, respectively. In Fig. S29,† the interaction between the intermediate products (*COOH and *OCHO) and 3Mo-$C_2N_1$ demonstrates pronounced charge accumulation or depletion, particularly evident in Fig. S29b,† indicating strong adsorption between the surfaces of OCHO and 3Mo-$C_2N_1$. Additionally, the DOS reveals numerous overlapping peaks between the p orbital of O and the d orbital of Mo, signifying a strong hybrid effect. Consequently, desorption and reduction to CO are facilitated at 3Mo-$C_2N_1$. Similarly, in Fig. S30,† the interaction between *COOH and *OCHO and 3Ti-$C_2N_1$ exhibits notable charge accumulation or depletion, particularly evident in Fig. S30b† with strong adsorption observed between *COOH and the sur-

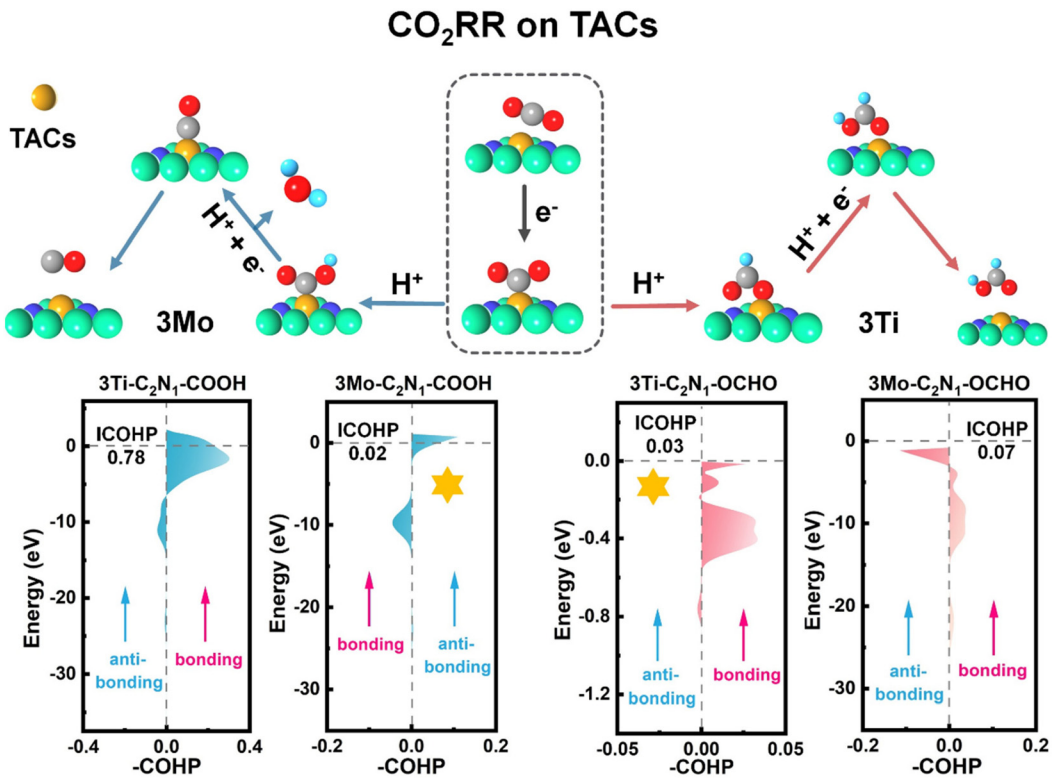


**Fig. 5** ICOHP values of *COOH and *OCHO on 3TM-$C_2N_1$.

faces of 3Ti-$C_2N_1$. Additionally, the DOS highlights numerous overlapping peaks between the p orbital of C and the d orbital of Ti, indicating a strong hybrid effect. Hence, desorption and reduction to HCOOH are facilitated at 3Ti-$C_2N_1$. Consequently, 3Mo-$C_2N_1$ and 3Ti-$C_2N_1$ demonstrate the best catalytic performance for $CO_2$ reduction to CO and HCOOH, respectively.

To further elucidate the interactions between atoms, we conducted COHP calculations. As depicted in Fig. 5, the bonding and anti-bonding regions between the 3TM and gas atoms are illustrated at the Fermi level, and the ICOHP values (absolute values) were plotted accordingly. For the CO product, it delineates a bonding region spanning from −2.3 eV to 1.2 eV and an anti-bonding region ranging from −12.5 eV to −16 eV between the metal Mo atom and the gas C atom with an ICOHP value of 0.02 eV. Furthermore, the bonding region between the metal Ti atom and the gas C atom spans from −6.6 eV to 2.4 eV with an anti-bonding region from −14.8 eV to −7.1 eV and an ICOHP value of 0.78 eV. As depicted in Fig. S28,† there is an ICOHP value of 0.01 eV between the metal Mn atom and the gas C atom and an ICOHP value of 0.53 eV between the metal Ru atom and the gas C atom. This indicates that the interaction between *C in the intermediate product *COOH and Mo atoms is moderate, thus ensuring the optimal performance of the 3Mo-$C_2N_1$ catalyst for CO generation.

For the HCOOH product, the bonding region between the metal Mo atom and the gas O atom extends from −13.8 eV to −2.7 eV, while the anti-bonding region ranges from −2.8 eV to −0.12 eV with an ICOHP value of 0.07 eV. Meanwhile, the bonding region between the metal Ti atom and the gas O atom ranges from −0.53 eV to 0 eV with an anti-bonding region from −0.88 eV to −0.67 eV and an ICOHP value of 0.03 eV. As depicted in Fig. S28,† there is an ICOHP value of 0.007 eV between the metal Mn atom and the gas O atom, and an ICOHP value of 0.25 eV between the metal Ru atom and the gas O atom. This indicates that the interaction between *O in the intermediate product *OCHO and the Ti atoms is moderate, thus ensuring the optimal performance of the 3Ti-$C_2N_1$ catalyst for HCOOH generation.

In addition, based on the relationship between the d-band center and the adsorption energy (as shown in Fig. 2b), the height of the d-band center of the catalyst material can be best regulated after the doping of three atoms. Therefore, TACs have a moderate adsorption energy for the intermediate products (*COOH and *OCHO), thus ensuring their optimal catalytic performance. In summary, these results demonstrate that 3Mo-$C_2N_1$ and 3Ti-$C_2N_1$ are the best catalysts for the formation of CO and HCOOH, respectively.

## 3. Conclusions

In summary, the mechanism of the $CO_2$RR on the SACs and SCCs of Mn, Mo, Ru and Ti anchored on the $C_3N_1$ monolayer was studied by DFT calculations. The results show that the TM-$C_2N_1$ catalysts are stable based on cohesion energy. Besides, AIMD was used to further verify the thermodynamic stability of the catalyst material. As an excellent electrocatalytic material, the conductivity of the TM-$C_2N_1$ monolayer was significantly improved based on the height of DOS at the Fermi level. Furthermore, the PDOS shows the obvious overlapping peaks between the d orbital of the TM and the p orbital of the N of the $C_2N_1$ monolayer, indicating that the TM can be stably anchored to the substrate. Importantly, $CO_2$ is significantly activated on the TM-$C_2N_1$ monolayer and the change in the bond angle is from 127.19° to 163.22°. At the same time, the catalyst can effectively prevent the side reaction of the HER. The good diffusion of the gas reactants is the initial condition for the $CO_2$RR, so the diffusion performance of $CO_2$ on the TM-$C_2N_1$ catalyst was calculated by molecular dynamics simulations. The results show that the 3Mo-$C_2N_1$ and 3Ti-$C_2N_1$ catalysts have the smallest diffusion coefficients of 2.19 and 2.78, respectively, and could stably adsorb $CO_2$ at active sites. Interestingly, 3Mo-$C_2N_1$ and 3Ti-$C_2N_1$ also exhibited the best catalytic activity for $CO_2$ reduction to CO and HCOOH, respectively. The pathway for the reduction of $CO_2$ to CO involves steps of $CO_2$ → *COOH → *CO → CO with a $U_L$ of −0.62 V. The pathway for $CO_2$ reduction to HCOOH was $CO_2$ → *OCHO → *HCOOH → HCOOH and $U_L$ is −0.42 V. In order to elucidate why the 3TM-$C_2N_1$ catalyst has the best catalytic performance, we established a volcano diagram relationship curve between $\eta$ and $E_{ads}$. The results emphasize the importance of moderate adsorption energy. In particular, the COHPs of *COOH and *OCHO for 3Mo-$C_2N_1$ and 3Ti-$C_2N_1$ catalysts were investigated in detail to compare the bonding and antibonding contributions. ICOHP shows that for CO, the ICOHP value of 3Mo-$C_2N_1$-COOH is 0.02 eV, and for HCOOH, the ICOHP value of 3Ti-$C_2N_1$-OCHO is 0.03 eV. It is proved that the optimum catalytic effect can be guaranteed only when the intermediate products have moderate adsorption energy. Therefore, this work provides theoretical guidance for the rational design of high-performance $CO_2$RR catalysts and offers new insights into understanding the catalytic mechanism of multi-atomic catalysts.

## Author contributions

Yimeng Sun: investigation, data curation, formal analysis, methodology, and writing – original draft. Lin Tao: investigation, data curation, methodology, supervision, funding acquisition, conceptualization, validation, and writing – review and editing. Mingjie Wu: methodology, resources, and writing – review and editing. Davoud Dastan: formal analysis and software. Javed Rehman: methodology and software. Lixiang Li: methodology and formal analysis. Baigang An: supervision, formal analysis, and writing – review and editing.

## Conflicts of interest

The authors declare that they have no known competing financial interests or personal relationships that could have appeared to influence the work reported in this paper.

## Acknowledgements

The funding from the National Natural Science Foundation of China (Grant No. 52304330, 52371224, and 22208331), the University of Science and Technology Liaoning Talent Project Grants (6003000317), the Outstanding Youth Fund of University of Science and Technology Liaoning (2023YQ11), and the Youth Fund of the Education Department of Liaoning Province (LJKQZ20222324) is gratefully acknowledged.

## References

1 T. Liu, Y. Wang and Y. Li, Can Metal–Nitrogen–Carbon Single-Atom Catalysts Boost the Electroreduction of Carbon Monoxide?, *JACS Au*, 2023, **3**, 943–952.
2 L. Tao, D. Dastan, W. Wang, P. Poldorn, X. Meng, M. Wu, H. Zhao, H. Zhang, L. Li and B. An, Metal-Decorated InN Monolayer Senses $N_2$ against $CO_2$, *ACS Appl. Mater. Interfaces*, 2023, **15**, 12534–12544.
3 S. Liu, M. Ge, L. Meng, X. Liu and T. Fang, Mechanism analysis of $CO_2$ separation from pvdf-supported deep eutectic solvent: A molecular dynamics simulation study, *J. Mol. Liq.*, 2024, **403**, 124806.
4 Y. Ouyang, L. Shi, X. Bai, C. Ling, Q. Li and J. Wang, Selectivity of Electrochemical CO2 Reduction toward Ethanol and Ethylene: The Key Role of Surface-Active Hydrogen, *ACS Catal.*, 2023, 15448–15456.
5 L. Tao, J. Huang, D. Dastan, T. Wang, J. Li, X. Yin and Q. Wang, New insight into absorption characteristics of $CO_2$ on the surface of calcite, dolomite, and magnesite, *Appl. Surf. Sci.*, 2021, **540**, 148320.
6 X. Li, X. Yu and Q. Yu, Research progress on electrochemical $CO_2$ reduction for Cu-based single-atom catalysts, *Sci. China Mater.*, 2023, **66**, 3765–3781.
7 L. Yu, F. Li, J. Huang, B. G. Sumpter, W. E. Mustain and Z. Chen, Double-Atom Catalysts Featuring Inverse Sandwich Structure for $CO_2$ Reduction Reaction: A Synergetic First-Principles and Machine Learning Investigation, *ACS Catal.*, 2023, 9616–9628.
8 L. Liu and H. Xiao, Inverted Region in Electrochemical Reduction of $CO_2$ Induced by Potential-Dependent Pauli Repulsion, *J. Am. Chem. Soc.*, 2023, **145**, 14267–14275.
9 Y. Zhang, T. Liu, X. Wang, Q. Dang, M. Zhang, S. Zhang, X. Li, S. Tang and J. Jiang, Dual-Atom Metal and Nonmetal Site Catalyst on a Single Nickel Atom Supported on a Hybridized BCN Nanosheet for Electrochemical $CO_2$ Reduction to Methane: Combining High Activity and Selectivity, *ACS Appl. Mater. Interfaces*, 2022, **14**, 9073–9083.
10 Y. Yan, Z. Zhao, J. Zhao, W. Tang, W. Huang and J.-M. Lee, Atomic-thin hexagonal CuCo nanocrystals with d-band tuning for $CO_2$ reduction, *J. Mater. Chem. A*, 2021, **9**, 7496–7502.
11 P. D. Pedersen, M. M. Melander, T. Bligaard, T. Vegge, K. Honkala and H. A. Hansen, Grand Canonical DFT Investigation of the $CO_2$RR and HER Reaction Mechanisms on $MoTe_2$ Edges, *J. Phys. Chem. C*, 2023, **127**, 18855–18864.
12 Z. Ma, T. Wan, D. Zhang, J. A. Yuwono, C. Tsounis, J. Jiang, Y.-H. Chou, X. Lu, P. V. Kumar, Y. H. Ng, D. Chu, C. Y. Toe, Z. Han and R. Amal, Atomically Dispersed Cu Catalysts on Sulfide-Derived Defective Ag Nanowires for Electrochemical $CO_2$ Reduction, *ACS Nano*, 2023, **17**, 2387–2398.
13 G. Wang, R. Ma, N. Zhang, Y. Guo and K. Chu, Single-atom Cu anchored on $Mo_2C$ boosts nitrite electroreduction to ammonia, *Chem. Commun.*, 2023, **59**, 13887–13890.
14 S. Ren, X. Cao, Z. Jiang, Z. Yu, T. Zhang, S. Wei, Q. Fan, J. Yang, J. Mao and D. Wang, Single-atom catalysts for electrochemical applications, *Chem. Commun.*, 2023, **59**, 2560–2570.
15 H. Zhu, Y. Feng, D. Zheng, X. Zhao, Y. Zhou, X. Fu, L. Zhao and X. Chen, Theoretical prediction of emerging high-performance trifunctional ORR/OER/HER single-atom catalysts: transition metals anchored into π–π conjugated graphitic carbon nitride (g-$C_{10}N_3$), *Phys. Chem. Chem. Phys.*, 2023, **25**, 31983–31994.
16 T. Zhang, L. Li, T. Huang, H. Wan, W.-Y. Chen, Z.-X. Yang, G.-F. Huang, W. Hu and W.-Q. Huang, Correlation between spin state and activity for hydrogen evolution of $PtN_2$ monolayer, *Appl. Phys. Lett.*, 2024, **124**(6), 063903.
17 W. Zou, R. Lu, X. Liu, G. Xiao, X. Liao, Z. Wang and Y. Zhao, Theoretical insights into dual-atom catalysts for the oxygen reduction reaction: the crucial role of orbital polarization, *J. Mater. Chem. A*, 2022, **10**, 9150–9160.
18 P. Kumar, K. Kannimuthu, A. S. Zeraati, S. Roy, X. Wang, X. Wang, S. Samanta, K. A. Miller, M. Molina, D. Trivedi, J. Abed, M. A. Campos Mata, H. Al-Mahayni, J. Baltrusaitis, G. Shimizu, Y. A. Wu, A. Seifitokaldani, E. H. Sargent, P. M. Ajayan, J. Hu and M. G. Kibria, High-Density Cobalt Single-Atom Catalysts for Enhanced Oxygen Evolution Reaction, *J. Am. Chem. Soc.*, 2023, **145**, 8052–8063.
19 T. Huang, Z.-X. Yang, L. Li, H. Wan, C. Leng, G.-F. Huang, W. Hu and W.-Q. Huang, Dipole Effect on Oxygen Evolution Reaction of 2D Janus Single-Atom Catalysts: A Case of Rh Anchored on the P6m2-NP Configurations, *J. Phys. Chem. Lett.*, 2024, **15**, 2428–2435.
20 Q. Pan, Y. Chen, S. Jiang, X. Cui, G. Ma and T. Ma, Insight into the active sites of M–N–C single-atom catalysts for electrochemical $CO_2$ reduction, *Energy Chem.*, 2023, 100114.
21 Q. Chang, Y. Liu, J.-H. Lee, D. Ologunagba, S. Hwang, Z. Xie, S. Kattel, J. H. Lee and J. G. Chen, Metal-Coordinated Phthalocyanines as Platform Molecules for Understanding Isolated Metal Sites in the Electrochemical Reduction of $CO_2$, *J. Am. Chem. Soc.*, 2022, **144**, 16131–16138.
22 S. Nie, J. Li, L. Tao, Y. He, D. Dastan, X. Meng, P. Poldorn and X. Yin, Insights into Selective Mechanism of NiO-$TiO_2$ Heterojunction to $H_2$ and CO, *ACS Sens.*, 2023, **8**, 4121–4131.
23 Y. Liu, L. Li, Q. Li, J. Lin, Z. Guo, X. Zhang, Z. Lu, Y. Ma, Y. Huang and C. Tang, Fluorine doped porous boron

nitride for efficient $CO_2$ capture and separation: A DFT study, *Appl. Surf. Sci.*, 2021, **556**, 149775.
24 X. Lu, Y. Hu, S. Cao, J. Li, C. Yang, Z. Chen, S. Wei, S. Liu and Z. Wang, Two-dimensional MBene: a comparable catalyst to MXene for effective $CO_2$RR towards $C_1$ products, *Phys. Chem. Chem. Phys.*, 2023, **25**, 18952–18959.
25 Z. Wang, B. N. DiMarco, M. Z. Ertem, R. N. Sampaio and G. F. Manbeck, Electronic and Electrochemical Control of Isostructural Ruthenium Hydricities and the Implications for Catalytic Overpotentials, *ACS Catal.*, 2024, 1419–1431.
26 M. Sadehvand, A. Amiri, A. Pazoki and F. F. Tirani, Electrochemically $CO_2$ conversion using homogeneous and nanostructured heterogeneous Ru(II) electrocatalysts, *Fuel*, 2023, **335**, 126712.
27 K. Peng, J. Ye, H. Wang, H. Song, B. Deng, S. Song, Y. Wang, L. Zuo and J. Ye, Natural halloysite nanotubes supported Ru as highly active catalyst for photothermal catalytic $CO_2$ reduction, *Appl. Catal., B*, 2023, **324**, 122262.
28 M. Pu, W. Guo and Y. Guo, Non-Noble Metal Incorporated Transition Metal Dichalcogenide Monolayers for Electrochemical $CO_2$ Reduction: A First-Principles Study, *ACS Appl. Mater. Interfaces*, 2023, **15**, 58388–58396.
29 C. Zhao, X. Su, S. Wang, Y. Tian, L. Yan and Z. Su, Single-atom catalysts on supported silicomolybdic acid for $CO_2$ electroreduction: a DFT prediction, *J. Mater. Chem. A*, 2022, **10**, 6178–6186.
30 X. Wang, L. Xu, C. Li, C. Zhang, H. Yao, R. Xu, P. Cui, X. Zheng, M. Gu, J. Lee, H. Jiang and M. Huang, Developing a class of dual atom materials for multifunctional catalytic reactions, *Nat. Commun.*, 2023, **14**, 7210.
31 J. Pan, X. E. Li, Y. Zhu, J. Zhou, Z. Zhu, C. Li, X. Liu, X. Liang, Z. Yang, Q. Chen, P. Ren, X. D. Wen, X. Zhou and K. Wu, Clustering-Evolved Frontier Orbital for Low-Temperature $CO_2$ Dissociation, *J. Am. Chem. Soc.*, 2023, **145**, 18748–18752.
32 Y. Zhao, D. Ma, J. Zhang, Z. Lu and Y. Wang, Transition metal embedded $C_3N$ monolayers as promising catalysts for the hydrogen evolution reaction, *Phys. Chem. Chem. Phys.*, 2019, **21**, 20432–20441.
33 Q. Bing and J.-Y. Liu, Transition metal single atom anchored $C_3N$ for highly efficient formic acid dehydrogenation: A DFT study, *Appl. Surf. Sci.*, 2021, **562**, 150186.
34 M. Gu, L. Tao, D. Dastan, J. Dang, T. Fang and B. An, Metal-Modified $C_3N_1$ Monolayer Sensors for Battery Instability Monitoring, *J. Mater. Chem. A*, 2024, DOI: **10.1039/d4ta00645c**.
35 Q. Zhang, D. Liu, Y. Zhang, Z. Guo, M. Chen, Y. Chen, B. Jin, Y. Song and H. Pan, Insight into coupled Ni-Co dual-metal atom catalysts for efficient synergistic electrochemical $CO_2$ reduction, *J. Energy Chem.*, 2023, **87**, 509–517.
36 J. Wu, D. Wu, H. Li, Y. Song, W. Lv, X. Yu and D. Ma, Tailoring the coordination environment of double-atom catalysts to boost electrocatalytic nitrogen reduction: a first-principles study, *Nanoscale*, 2023, **15**, 16056–16067.
37 C. Chen, M. Sun, K. Wang and Y. Li, Dual–metal single–atomic catalyst: The challenge in synthesis, characterization, and mechanistic investigation for electrocatalysis, *SmartMat*, 2022, **3**, 533–564.
38 D. Ma, Y. Wang, L. Liu and Y. Jia, Electrocatalytic nitrogen reduction on the transition-metal dimer anchored N-doped graphene: performance prediction and synergetic effect, *Phys. Chem. Chem. Phys.*, 2021, **23**, 4018–4029.
39 Y. Wang, B. J. Park, V. K. Paidi, R. Huang, Y. Lee, K.-J. Noh, K.-S. Lee and J. W. Han, Precisely Constructing Orbital Coupling-Modulated Dual-Atom Fe Pair Sites for Synergistic $CO_2$ Electroreduction, *ACS Energy Lett.*, 2022, **7**, 640–649.
40 Y. Li, Y. Chen, Z. Guo, C. Tang, B. Sa, N. Miao, J. Zhou and Z. Sun, Breaking the linear scaling relations in MXene catalysts for efficient $CO_2$ reduction, *Chem. Eng. J.*, 2022, **429**, 132171.
41 H. T. D. Bui, V. Q. Bui, S. G. Kim, Y. Kawazoe and H. Lee, Revealing well-defined cluster-supported bi-atom catalysts for enhanced $CO_2$ electroreduction: a theoretical investigation, *Phys. Chem. Chem. Phys.*, 2021, **23**, 25143–25151.
42 S. Wang, M. Luo and S. Guo, Two atoms are better than one, *Nat. Synth.*, 2022, **1**, 676–677.
43 M. Jiao, Z. Chen, N. Wang and L. Liu, DFT calculation screened CoCu and CoFe dual-atom catalysts with remarkable hydrogen evolution reaction activity, *Appl. Catal., B*, 2023, **324**, 122244.
44 C. Yang, Y. Wu, Y. Wang, H.-N. Zhang, L.-H. Zhu and X.-C. Wang, Electronic properties of double-atom catalysts for electrocatalytic oxygen evolution reaction in alkaline solution: a DFT study, *Nanoscale*, 2022, **14**, 187–195.
45 S. Li, L. Tong, Z. Peng, B. Zhang and X. Fu, Efficient $CO_2$ reduction for CO production using triatomic catalyst screening: A DFT study, *Appl. Surf. Sci.*, 2024, **644**, 158804.
46 P. V. Bakharev, M. Huang, M. Saxena, S. W. Lee, S. H. Joo, S. O. Park, J. Dong, D. C. Camacho-Mojica, S. Jin, Y. Kwon, M. Biswal, F. Ding, S. K. Kwak, Z. Lee and R. S. Ruoff, Chemically induced transformation of chemical vapour deposition grown bilayer graphene into fluorinated single-layer diamond, *Nat. Nanotechnol.*, 2019, **15**, 59–66.
47 M. Wu, F. Dong, Y. Yang, X. Cui, X. Liu, Y. Zhu, D. Li, S. Omanovic, S. Sun and G. Zhang, Emerging Atomically Precise Metal Nanoclusters and Ultrasmall Nanoparticles for Efficient Electrochemical Energy Catalysis: Synthesis Strategies and Surface/Interface Engineering, *Electrochem. Energy Rev.*, 2024, **7**, 10.
48 Y. Wang, J. Zhang, J. Zhao, Y. Wei, S. Chen, H. Zhao, Y. Su, S. Ding and C. Xiao, Strong Hydrogen-Bonded Interfacial Water Inhibiting Hydrogen Evolution Kinetics to Promote Electrochemical $CO_2$ Reduction to $C_{2+}$, *ACS Catal.*, 2024, **14**, 3457–3465.
49 S. Li, M. Shi, C. Wu, K. Nie, Z. Wei, X. Jiang, X. Liu, H. Chen, X. Tian, D. Wu and Y. Li, Surface addition of Ag on $PbO_2$ to enable efficient oxygen evolution reaction in pH-neutral media, *Chem. Eng. J.*, 2024, **485**, 150043.
50 S. Jia, Q. Zhu, H. Wu, S. Han, M. Chu, J. Zhai, X. Xing, W. Xia, M. He and B. Han, Preparation of trimetallic electrocatalysts by one-step co-electrodeposition and efficient $CO_2$ reduction to ethylene, *Chem. Sci.*, 2022, **13**, 7509–7515.

51 W. Liu, J. Liu, Y. Yang, B. Xiong and H. Bai, Tunable trimetallic TM-NiFe catalysts for enhancing the products selectivity of $CO_2$ electroreduction, *Fuel*, 2023, **335**, 127026.
52 J.-C. Liu, H. Xiao, X.-K. Zhao, N.-N. Zhang, Y. Liu, D.-H. Xing, X. Yu, H.-S. Hu and J. Li, Computational Prediction of Graphdiyne-Supported Three-Atom Single-Cluster Catalysts, *CCS Chem.*, 2023, **5**, 152–163.
53 L. Yang, S. Feng and W. Zhu, Achieving reaction pathway separation for electrochemical nitrate fixation on triatomic catalysts: A new mechanism, *J. Hazard. Mater.*, 2023, **441**, 129972.
54 S. Nie, L. Tao, J. Li, W. Wang, P. Poldorn, Y. He, X. Yin and M. Wu, A single response to reducing gases by NiO-$TiO_2$ heterojunction nanocrystals, *Appl. Surf. Sci.*, 2024, **644**, 158821.
55 Y. He, L. Tao, J. Li, M. Wu, P. Poldorn, D. Dastan, S. Abbasi, S. Nie, X. Yin and Q. Wang, Atomic-level insights into selective adsorption of $H_2$ and CO on $SnO_2$/CoO heterojunctions, *Mater. Today Nano*, 2023, **22**, 100334.
56 L. Tao, J. Huang, D. Dastan, T. Wang, J. Li, X. Yin and Q. Wang, $CO_2$ capture and separation on charge-modulated calcite, *Appl. Surf. Sci.*, 2020, **530**, 147265.
57 I. S. Amiinu, X. Liu, Z. Pu, W. Li, Q. Li, J. Zhang, H. Tang, H. Zhang and S. Mu, From 3D ZIF Nanocrystals to Co-$N_x$/C Nanorod Array Electrocatalysts for ORR, OER, and Zn-Air Batteries, *Adv. Funct. Mater.*, 2018, **28**, 1704638.
58 M. Wang, W. Ma, C. Tan, Z. Qiu, L. Hu, X. Lv, Q. Li and J. Dang, Designing Efficient Non-Precious Metal Electrocatalysts for High-Performance Hydrogen Production: A Comprehensive Evaluation Strategy, *Small*, 2023, e2306631.
59 Y. He, J. Li, L. Tao, S. Nie, T. Fang, X. Yin and Q. Wang, First-principles calculations on the resistance and electronic properties of H2 adsorption on a CoO-$SnO_2$ heterojunction surface, *Phys. Chem. Chem. Phys.*, 2021, **24**, 392–402.
60 Z. Lv, W. Ma, M. Wang, J. Dang, K. Jian, D. Liu and D. Huang, Co–Constructing Interfaces of Multiheterostructure on MXene ($Ti_3C_2T_x$)–Modified 3D Self–Supporting Electrode for Ultraefficient Electrocatalytic HER in Alkaline Media, *Adv. Funct. Mater.*, 2021, **31**, 2102576.
61 K. Boonpalit, J. Kinchagawat, C. Prommin, S. Nutanong and S. Namuangruk, Efficient exploration of transition-metal decorated MXene for carbon monoxide sensing using integrated active learning and density functional theory, *Phys. Chem. Chem. Phys.*, 2023, **25**, 28657–28668.
62 R. Dagan, Y. Vaknin and Y. Rosenwaks, Gap state distribution and Fermi level pinning in monolayer to multilayer $MoS_2$ field effect transistors, *Nanoscale*, 2020, **12**, 8883–8889.
63 L. Tao, J. Huang, X. Yin, Q. Wang, Z. Li, G. Wang and B. Cui, Adsorption Kinetics of $CO_2$ on a Reconstructed Calcite Surface: An Experiment-Simulation Collaborative Method, *Energy Fuels*, 2019, **33**, 8946–8953.
64 L. Tao, J. Huang, D. Dastan, J. Li, X. Yin and Q. Wang, Flue gas separation at organic-inorganic interface under geological conditions, *Surf. Interfaces*, 2021, **27**, 101462.
65 Y.-Q. Wang, X.-H. Dan, Z.-Y. Yi, X. Wang, Y.-C. Feng, Y. Feng, D. Wang and L.-J. Wan, Single-Molecule Study on the Catalytic Role of Co–$O_2$ Binding in ORR by In Situ ECSTM, *J. Phys. Chem. C*, 2023, **127**, 2929–2935.
66 P. Sun, S. Liu, X. Zheng, G. Hu, Q. Zhang, X. Liu, G. Zheng and Y. Chen, Challenges and opportunities of atomic-scales reactive sites in thriving electrochemical $CO_2$ reduction reaction, *Nano Today*, 2024, **55**, 102152.
67 G. Yasin, A. Kumar, S. Ajmal, M. Asim Mushtaq, M. Tabish, A. Saad, M. A. Assiri, M. Tariq Nazir and Q. Zhuo, Advances and perspectives on heteronuclear dual-atomic catalysts for prevailing the linear scaling relationship in electrocatalytic $CO_2$ reduction, *Coord. Chem. Rev.*, 2024, **501**, 215589.
68 R. Zhu, Y. Qin, T. Wu, S. Ding and Y. Su, Insights into local coordination environment of main group metal-nitrogen-carbon catalysts for enhanced oxygen reduction reaction, *Appl. Surf. Sci.*, 2023, **631**, 157581.
69 L. Diao, B. Zhang, Q. Sun, N. Wang, N. Zhao, C. Shi, E. Liu and C. He, An in-plane $Co_9S_8$@$MoS_2$ heterostructure for the hydrogen evolution reaction in alkaline media, *Nanoscale*, 2019, **11**, 21479–21486.